water

MDPI

Article

Visible Light-Driven Photocatalytic Degradation of Tetracycline Using p-n Heterostructured Cr_2O_3/ZrO_2 Nanocomposite

Xueyu Wei [1,*], Saraschandra Naraginti [2,*], Pengli Chen [1,3], Jiyuan Li [1], Xiaofan Yang [2] and Buwei Li [1]

[1] School of Civil Engineering and Architecture, Anhui Polytechnic University, Wuhu 241000, China
[2] School of Chemical and Environmental Engineering, Anhui Polytechnic University, Wuhu 241000, China; xiaofan108@ahpu.edu.cn
[3] Jiangsu Academy of Environmental Industry and Technology Corp, Nanjing 210036, China
* Correspondence: wxyu1027@126.com (X.W.); saras@mail.ahpu.edu.cn (S.N.)

Abstract: Antibiotic pollution beyond the safety limits poses a significant threat to the environmental sustainability and human health which necessitates the development of efficient methods for reducing antibiotics in pharmaceutical wastewater. Photocatalysis is a proven technology which has drawn considerable attention in semiconductor photocatalysts. Our study aims to develop a highly efficient Cr_2O_3/ZrO_2 photocatalyst for the degradation of tetracycline (TCL) under visible light. The synthesized catalyst was well characterized by XRD, HR-TEM-SAED, XPS, FT-IR, BET and UV-Vis-DRS methods. The effects of various parameters on photocatalytic degradation were evaluated in detail, showing that 97.1% of 50 mgL^{-1} tetracycline concentrations could be degraded within 120 min at pH 5 with a 0.1 gL^{-1} photocatalyst-loading concentration under visible light (300 W Xe lamp). The uniform distribution of spherical ZrO_2 nanoparticles on the surface of the Cr_2O_3 nano-cubes efficiently reduced the recombination rate with an energy bandgap of 2.75 eV, which provided a faster photodegradation of tetracycline under visible light. In addition, a plausible degradation pathway and photoproducts generated during the photocatalytic degradation of TCL are proposed based on the LC-ESI/MS results, which suggested that efficient photodegradation was achieved during the visible light irradiation. Thus, our study reveals that the cost-effective Cr_2O_3-based photocatalyst with multi-reusability and efficient energy consumption could be an efficient photocatalyst for the rapid degradation of TCL during the wastewater treatment process.

Keywords: Cr_2O_3/ZrO_2; visible light; tetracycline; degradation; photocatalysis

Citation: Wei, X.; Naraginti, S.; Chen, P.; Li, J.; Yang, X.; Li, B. Visible Light-Driven Photocatalytic Degradation of Tetracycline Using p-n Heterostructured Cr_2O_3/ZrO_2 Nanocomposite. *Water* **2023**, *15*, 3702. https://doi.org/10.3390/w15203702

Academic Editor: Meimei Zhou

Received: 23 September 2023
Revised: 17 October 2023
Accepted: 19 October 2023
Published: 23 October 2023

1. Introduction

In the recent past, ecological imbalance has become a major environmental issue caused by the contamination of surface water due to rapid industrial development and the littering of household waste [1]. Several studies have demonstrated that chemical compounds released from pharmaceutical industries are known to be highly toxic and hazardous to aquatic ecosystems when they are left untreated [2,3]. In this context, tetracycline (TCL) belongs to the group of phenanthrene core antibiotics that are widely used to treat Gram-positive and Gram-negative bacteria, growth promoters for animals, intracellular mycoplasma, chlamydia, and rickettsia infections. Consequently, more than 50% of these antibiotics end up in the environment after they have been consumed by humans and animals [4]. The release of these antibiotic residues and their metabolites into the aquatic environment contributes to the rise in antibiotic resistance genes in the aquatic life and has had a significant influence on the environment. The high hydrophilicity of these compounds not only makes them biologically toxic for aquatic species but also enriches and transmits them through the food chain, resulting in serious health concerns for humans [5]. Due to the higher concentrations of these contaminates, clean water has also become scarce for humans and the environment [6]. Globally, the current unsafe situation has become a

major concern, and it is expected to become worse as time goes on [7]. Thus, developing low-cost and efficient wastewater treatment technologies is urgently needed to combat this growing problem [8,9]. However, adsorption and coagulation processes are considered ineffective for conventional wastewater treatment systems due to their high operational costs and significant energy demands [10,11]. Furthermore, these existing water treatment methods are largely unfruitful due to high salinity and secondary pollutants [12].

The photocatalytic oxidation process is a well-known technology and a viable alternative to conventional wastewater treatment [13]. Through the usage of solar light as the source of energy and high-activity metal-oxide nanoparticles as the processing input, it is capable of degrading organic pollutants such as tetracycline in a sustainable manner [14]. Semiconductor photocatalysis which utilizes solar energy has drawn significant attention in the global scientific community due to its great potential in the search for better solutions to current environmental and energy issues [15]. This has led to the development of several nanomaterials like g-C_3N_4, $FeAl_2O_4$, Cu_2O, Bi_2WO_6, CdS-N/ZnO, etc., for the photocatalytic degradation of various organic pollutants under visible light [16–20]. However, all these methods have limitations, such as high costs, slow degradation rates, UV-active materials, and reusability issues. Hence, in recent years, there has been increasing interest in the development of simple, cost-effective p-n heterojunction semiconductors that can be used as solar-harvesting photocatalysts to degrade TCL pollutants [21].

Following this, Cr_2O_3 is a widely recognized flagship p-type semiconducting material that can be used for photocatalysis enhancement. Furthermore, the strategic selection of Cr_2O_3 is based on a waste-to-resources conversion strategy, in which carcinogenic hexavalent chromium compounds that are utilized in various industrial applications can be converted into benign trivalent chromium oxide that can be used as a photocatalyst for environmental remediation. Thus, Cr_2O_3 has been envisioned as an alternative photoactive material through a modified method of coupling it with a stable metal oxide. For instance, Singh et al. proposed a new Fe_3O_4-Cr_2O_3 magnetic nanocomposite prepared using a simple wet chemical method for degradation of 4-chlorophenol under UV light [22]. Similarly, Ahmed et al. used sol–gel synthesis to prepare spherical mesoporous Cr_2O_3-TiO_2 nanoparticles, and with UV light exposure, the photocatalyst exhibited 90.0% efficiency in removing methylene blue dye [23]. Consequently, due to its high rate of electron–hole recombination, Cr_2O_3 is widely employed as a co-catalyst in conjunction with other semiconducting materials. Hence, to overcome these drawbacks and make Cr_2O_3 a visible active photocatalyst, it must be coupled to a semiconducting material with a slightly higher bandgap [24]. As an n-type semiconductor, ZrO_2 is becoming a widely used material in photocatalysis [25]. The unique properties of ZrO_2 that include high refractive index, high thermal expansion, high optical transparency, chemical and photothermal stability, excellent corrosion resistance, and low thermal conductivity have led to its extensive use in photocatalysis in recent years [26]. However, its large bandgap of 3.87 eV and high electron–hole recombination rate makes ZrO_2's photocatalytic activity limited to the UV range [27]. Interestingly, several recent studies have demonstrated that the combination of various other metal oxides with ZrO_2 to form a heterojunction would eventually increase its visible-light-active efficiency during the degradation process [28].

In response to these observations, we synthesized a stable and efficient heterostructure Cr_2O_3/ZrO_2 catalyst via the coprecipitation method. The photocatalyst ensures $\geq$ 97.1% TCL degradation led by hydroxyl and superoxide radical species. The superior analytical performance and reusability of the proposed nanocomposite materials make them an attractive choice for environmental remediation applications in the antibiotic wastewater treatment process.

2. Materials and Methods

2.1. Synthesis of Cr_2O_3 Nano-Cubes

Firstly, to synthesize pure chromium oxide cubes, chromium (III) nitrate nonahydrate ($\geq$99.99%; Sigma Aldrich, Shanghai, China) was used as the precursor. In the initial process,

the Cr starting material (0.1 M) was mixed constantly for about 0.5 h, followed by the dropwise addition of ammonia (0.3 M) to control the pH 6.0, to obtain a green-colored precipitate. Then, the precipitate was separated and washed several times with deionized water in order to remove any soluble impurities. After obtaining chromium hydroxide precipitate, it was dried for 24 h at 90 °C followed by calcination at 900 °C for 5 h to obtain the chromium oxide cubes with an intense green color.

2.2. Preparation of Cr_2O_3-ZrO_2 Nanocomposite

To prepare the Cr_2O_3/ZrO_2 nanocomposite, the co-precipitation approach was employed. Initially, zirconium (IV) tetra-butoxide (≥99.99%; Sigma Aldrich, Shanghai, China) precursor was mixed with 15 mL solution of H_2O_2 (30% w/v), followed by stirring for 0.5 h, resulting in a white-colored colloidal peroxo complex of Zirconium. To the above suspension, 50 mL of distilled water and 0.25 g of previously synthesized Cr_2O_3 cubes were added, and the suspension was stirred for 24 h. Further, the complete suspension was then transferred to a Teflon-lined autoclave maintained at 100 °C for 12 h. After bringing the autoclave to room temperature, the catalyst was washed several times with water, dried at 80 °C, followed by calcination at 500 °C for 2 h at a ramp rate of 5 °C/min. The final powder was denoted as a Cr_2O_3/ZrO_2 nanocomposite. For comparison, the pure ZrO_2 nanoparticles were synthesized by following the same above-mentioned method without addition of Cr_2O_3 cubes.

2.3. Instrumentations

Several instruments have been used to characterize the as-synthesized photocatalytic materials. The wide angel XRD pattern for the synthesized photocatalyst materials were recorded using a BRUKER D8 Advance X-ray diffractometer (Karlsruhe, Germany) with 2θ ranges from 10° to 90°. The structural pattern and surface morphology of the prepared nanocomposite materials was studied using HR-TEM-SAED (Thermo Fisher Talos F200S G2 electron microscopes; Pleasanton, CA, USA). The energy band gap measurements for the prepared nanocomposites were calculated using a UV-Visible spectrophotometer equipped with diffused reflectance integrating sphere (DRS) (Shimadzu UV-360; Kyoto, Japan). An X-ray photoelectron spectrometer (XPS) (Thermo Scientific K-AlphaX; Pleasanton, CA, USA) with monochromatic Al Kα radiation (150 W, 15 kV, and 1486.74 eV) was used to study the oxidation states and surface composition of the prepared photocatalyst materials. FT-IR spectral measurements were carried out using a Thermo Scientific (Pleasanton, CA, USA) Nicolet iS10 model. BET analysis was carried out using a Kubo-X1000 high-performance micropore analyzer (Bbbm024; Shenzhen, China).

2.4. Photocatalytic Methodology

Photocatalytic activity of the Cr_2O_3/ZrO_2 catalyst was assessed in terms of degradation of TCL. The experiment was conducted in a laboratory-scale photocatalytic chamber equipped with a 300 W Xe lamp (simulated solar light). Initially, 100 mg of the photocatalyst was suspended in 100 mL of an aqueous solution containing 50 mgL^{-1} TCL. To eliminate the background reductions (adsorption/desorption) in TCL drug concentrations, the tubes containing TCL solutions and photocatalyst material were stirred in dark conditions for 20 min. The degradation efficiency of the samples was measured by collecting 2.5 mL aliquots at fixed intervals during irradiation. Before HPLC analysis, 2 mL of the sample was centrifuged, then filtered through 0.2 mm syringe filters. To monitor the decrease in TCL concentration, the withdrawn samples were analyzed using HPLC at its characteristic absorbance of 354 nm with an UV detector, while acetonitrile (30% v/v) and water (70% v/v) were used as the mobile phase at a flow rate of 1 mL min^{-1}. Meanwhile, the HPLC that connected to a tandem mass spectrophotometer (LC-ESI/MS/MS) was used to identify the degradation products during degradation. The ESI method was used in identifying the mass, helium gas was utilized at a flow rate ~1 mL min^{-1}, and a 16 V of fragment voltage was maintained during analysis. We followed the same procedure under

visible light irradiation to optimize various physiochemical parameters that may influence degradation efficiency.

3. Results and Discussion

3.1. Characterization

To determine the crystal structure and phase orientation of the prepared nanomaterials, XRD analysis was performed. Figure 1 illustrates the wide range of XRD patterns of Cr_2O_3, ZrO_2, and Cr_2O_3/ZrO_2 NCs materials as well as their JCPDS card patterns. The XRD diffraction pattern of the synthesized Cr_2O_3 nanoparticles observed at respective 2θ values and the corresponding indexed planes are 2θ = 24.80 (0 1 2), 33.82 (1 0 4), 35.80 (1 1 0), 41.17 (0 0 6), 42.73 (1 1 3), 45.53 (2 0 2) 51.43 (0 2 4), 56.30 (1 1 6), 59.41 (0 1 8), 62.80 (2 1 4), and 64.95 (3 0 0). These reflection planes indicated that the synthesized nanoparticles have a rhombohedral phase with an R3c space group, in accordance with the JCPDS Card No. 85-0869. In the same manner, the diffraction peaks of the pure ZrO_2 NPs reveal the peaks with the following values 2θ = 28.8 (−11.1), 32.01 (−11.1), 50.10 (12.2), and 61.76 (−13.1) indicating that the ZrO_2 is in monoclinic phase (JCPDS Card No. 37-1484). As a result of coupling the ZrO_2 with Cr_2O_3, no significant change in the peak position of the Cr_2O_3 lattice planes was observed, and both the rhombohedral and monoclinic distribution were clearly visible in the Cr_2O_3-ZrO_2 nanocomposite, indicating that ZrO_2 had no effect on the Cr_2O_3 matrix. This observation confirms that ZrO_2 was deposited only on the Cr_2O_3 NP surface, possibly because Zr^{4+} has a larger ionic radius than Cr^{3+}. Furthermore, peaks corresponding to ZrO_2 and Cr_2O_3 are clearly observed on the nanocomposite, indicating that no other detectable impurities are present. In addition, the Debye–Scherrer equation $D = K\lambda/\beta \cos\theta$ was applied to further determine the average crystalline size for the nanocomposite, in which β represents the full width at half maximum (FWHM) of the diffraction peak, θ indicates the angle between the incident and diffracted beams, λ specifies the wavelength of X-ray beam (1.540 Å for CuKα), and K is the shape factor (0.9). The crystalline size of the prepared composite has been carried out using the major intense peaks and their average size has been calculated as mentioned above. The crystalline size of the Cr_2O_3, ZrO_2, and Cr_2O_3/ZrO_2 nanocomposite was found to be around 30.91, 25.84, and 27.50, respectively.

The light absorption properties of the as-prepared catalysts were investigated using diffuse reflectance UV-Vis spectroscopy (UV-Vis-DRS). The spectral results indicated that Cr_2O_3 enhanced ZrO_2 absorption in the visible region, with a slight redshift in the absorption edge. This indicates that the Cr_2O_3/ZrO_2 heterostructure photocatalysts have effective activity in the visible range. Due to its octahedral geometrical preferences, the absorption spectra for pure Cr_2O_3 NPs exhibits three major peaks. This is the reason for the curved wave pattern in Tauc's plot of the corresponding band gap energy of the Cr_2O_3 NPs. The band gap energy of the nanocomposite (Cr_2O_3/ZrO_2) was calculated using Tauc's plot using the formula: $\alpha h\nu = A (h\nu - Eg) n$. Where A is constant, Eg represents band gap energy, the exponent $n = \frac{1}{2}$ for direct band gap transition, hν is photon energy, and α is the attenuation constant. According to the results, the energy band gaps of pristine Cr_2O_3, ZrO_2, and Cr_2O_3/ZrO_2 are found to be 2.12, 3.81, and 2.75 eV, respectively (Figure 2a). As a result of these increased absorptions as well as the reduced band gap energy in ZrO_2, the photocatalyst obtained higher efficiency under the visible light illumination.

The presence of multiple functional groups in pure Cr_2O_3, ZrO_2, and Cr_2O_3/ZrO_2 nanocomposites was confirmed by FT-IR analysis (Figure 2b). From the results, it shows that the strong vibration at 540 cm^{-1} was assigned to pristine Cr_2O_3 that indicates the presence of a Cr-O bond, while the strong vibration at 620 cm^{-1} was ascribed to the Cr_2O_3 crystalline peak. Similarly, the strong vibration peak at 530 cm^{-1} could be assigned to the Zr-O bond in pristine ZrO_2. As a result of the intervening peak at 530 cm^{-1} of ZrO_2 in Cr_2O_3/ZrO_2 nanocomposites, a peak broadening was observed for the twin peaks (540 cm^{-1} and 620 cm^{-1}) of Cr_2O_3. This further supports the formation of Cr_2O_3/ZrO_2 nanocomposites. A sharp band that appeared on all three peaks at 1620 cm^{-1} may be related

to the bending mode of hydroxyl groups from the surface-adsorbed molecules [29–31]. As a result of the formation of heterostructures, atmospheric CO_2 will react with the surface hydroxyl groups of Cr_2O_3/ZrO_2, which will result in the consumption of hydroxyl groups at vibrational band at 3450 cm^{-1}. These FTIR results are in complete agreement with our XRD results.

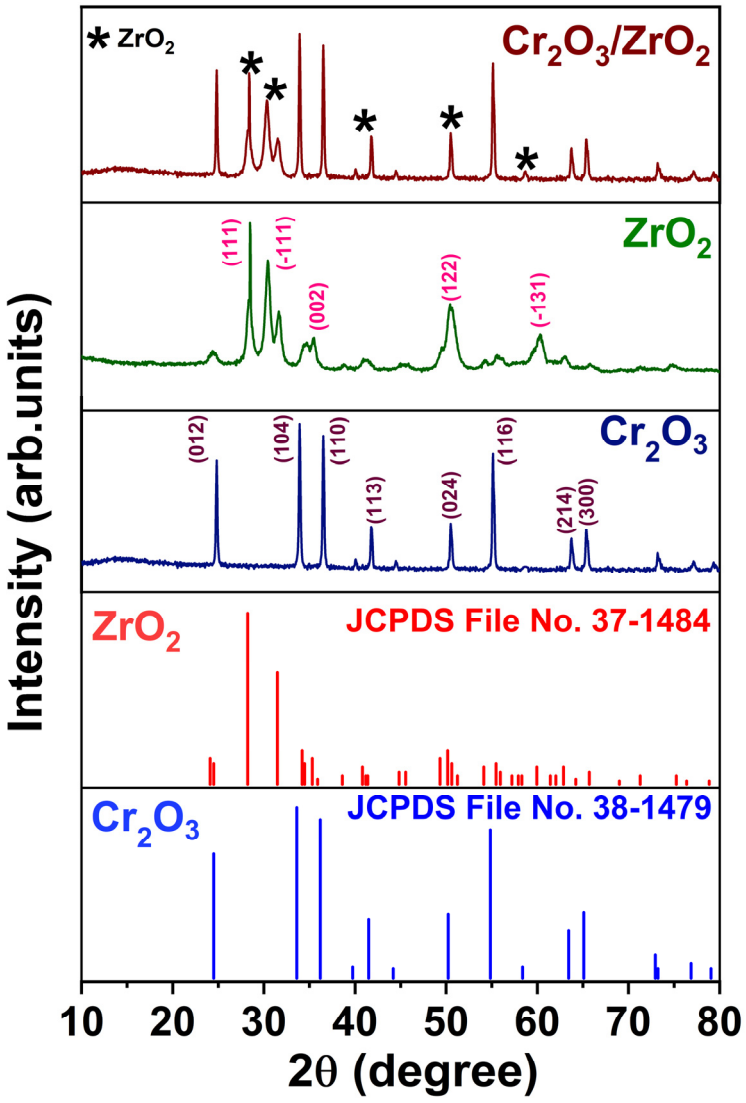

Figure 1. p-XRD pattern of pure Cr_2O_3, ZrO_2, and Cr_2O_3-ZrO_2 nanocomposites.

The morphological characteristics of the synthesized composite were investigated through HR-TEM. The results clearly evidenced that Cr_2O_3 are in nano-cubes (Figure 3a), while ZrO_2 are in slightly agglomerated particles (Figure 3b). It is evidenced that there is a formation of a Cr_2O_3/ZrO_2 heterojunction during the coprecipitation process as it can be seen from the images that the Cr_2O_3 nano-cubes are clearly visible and the ZrO_2 nanoparticles are agglomerated with equal distribution under Cr_2O_3 nano-cubes (Figure 3c). In addition, the average particle size of Cr_2O_3, ZrO_2, and Cr_2O_3/ZrO_2 NCs was calculated, and the corresponding values are about 36.5 nm, 27.5 nm, and 30.5 nm, respectively [10,32]. Additionally, the high-magnification TEM images clearly revealed that the lattice fringes of Cr_2O_3 and ZrO_2 with d-spacing values are about 0.332 and 0.237 nm (Figure 3d,e). Likewise, the SAED analysis of Cr_2O_3/ZrO_2 composite confirms the microcrystalline phase and the indexed planes match the p-XRD analysis (Figure 3f). With these morphological

features, it could be suggested that better adsorption and diffusion of TCL analytes are achievable, which enables effective removal under visible light.

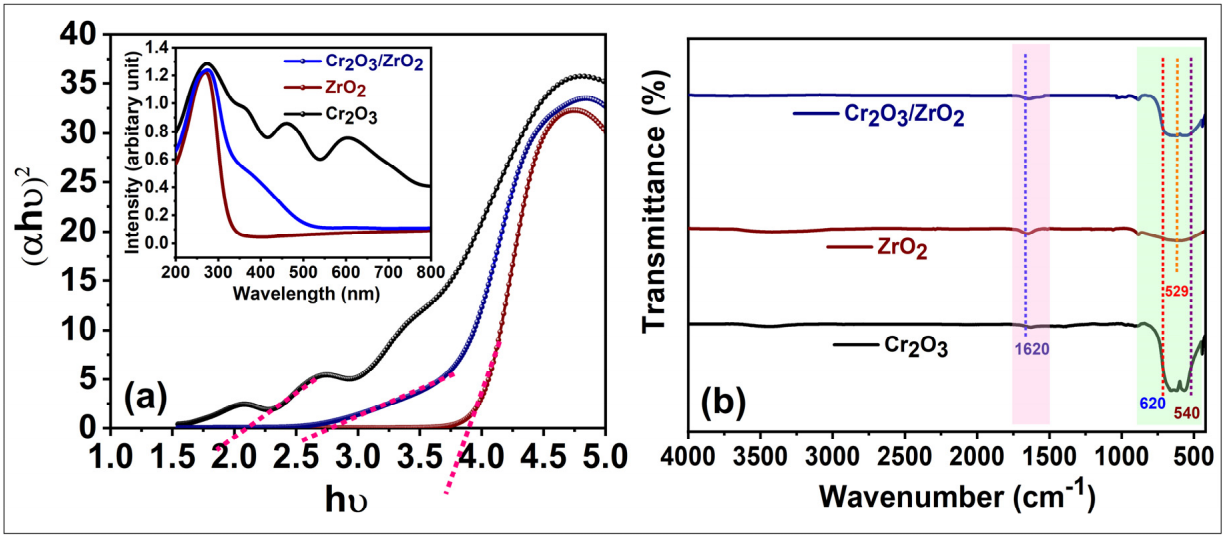

Figure 2. (**a**) Tauc plot (inset: UV-vis absorption spectra) and (**b**) FT-IR spectra of pure Cr_2O_3, ZrO_2 and Cr_2O_3–ZrO_2 nanocomposites.

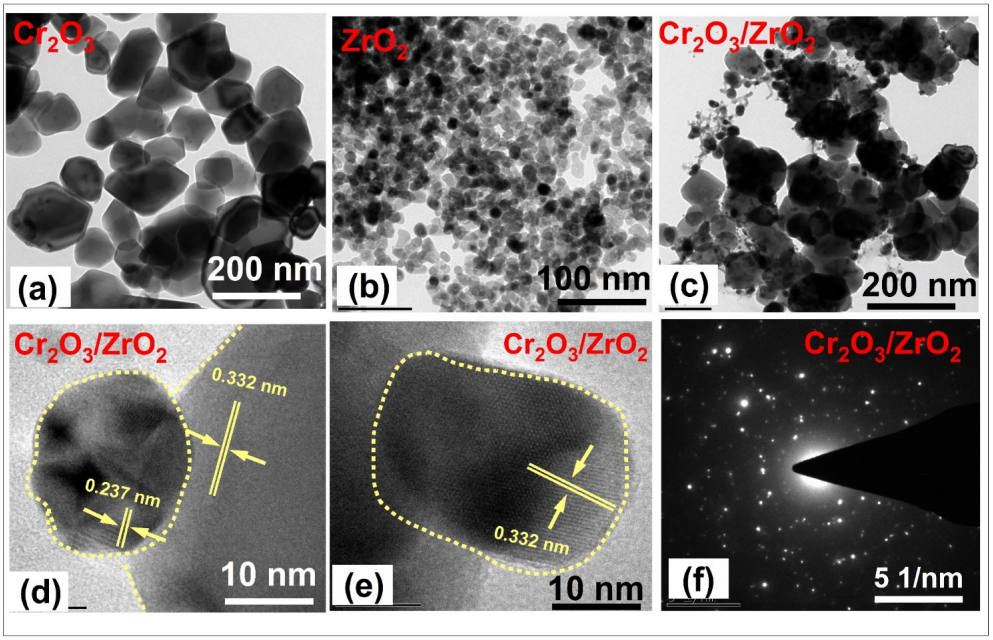

Figure 3. TEM images of (**a**) Cr_2O_3, (**b**) ZrO_2, and (**c**) Cr_2O_3–ZrO_2; (**d**,**e**) HR-TEM images and (**f**) SAED pattern of Cr_2O_3–ZrO_2 nanocomposites.

Surface composition, purity, and elemental analysis were carried out by X-ray photoelectron spectroscopy (XPS) for the as-prepared composite catalyst. From the results, it can be seen from the survey scan spectrum of the Cr_2O_3/ZrO_2 nanocomposite which showed all the elements of the composite and confirms their uniform distribution in the composite (Figure 4a). Accordingly, the Cr_2O_3/ZrO_2 nanocomposite exhibited high-intensity peaks at 180.32 eV, 580.25 eV, and 530.87 eV, ascribed to Zr 3d, Cr 2P, and O 1s, respectively. It is worth mentioning that the absence of the N 1s peak suggests that the NO^{3-} ion has been successfully removed from the precursor $Cr(NO_3)9H_2O$ during the synthesis and calcination process. The high-resolution Cr 2p spectrum (Figure 4b) shows two well-resolved peaks at

574.6 and 584.7 eV corresponding to Cr $2p_{3/2}$ and Cr $2p_{1/2}$ peaks, respectively. In addition, the energy separation of 9.8 eV between the $2p_{3/2}$ and $2p_{1/2}$ peaks indicated that the Cr 2p orbital contains chromium in a trivalent state (Cr^{3+}). Likewise, the deconvoluted Zr 3d orbital (Figure 4c) shows distinct states of Zr $3d_{3/2}$ and Zr $3d_{5/2}$, with binding energies of 198.8 eV and 182.1 eV, respectively, indicating an oxidation state of Zr^{4+}. Furthermore, the O 1s high resolution spectrum (Figure 4d) displays a former peak at 529.6 eV, that is assigned to the lattice oxygen of the composite, while the other intense peak at 532.3 eV could be ascribed to the OH species that result from the chemisorbed water [33–36]. According to the XPS results, the atomic percentages of the nanocomposite elements are found to be chromium (Cr^{3+})—25.5%, zirconium (Zr^{4+})—12.3%, oxygen (O)—41.7% and carbon (C)—20.5%, confirming the uniform distribution of the elements and the formation of a heterostructure between them.

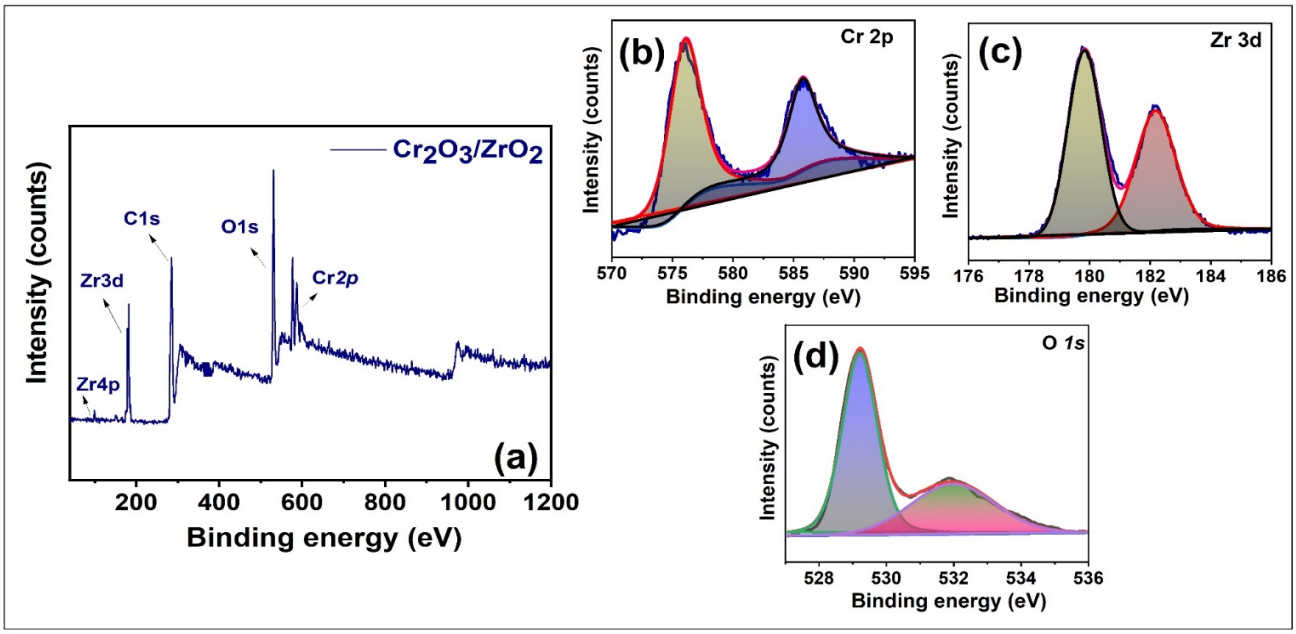

Figure 4. (**a**) XPS survey spectra of Cr_2O_3/ZrO_2 nanocomposite, and (**b**–**d**) high resolution deconvoluted XPS spectra for Cr 2p, Zr 3d, and O 1s orbitals.

In addition, the BET and pore size distribution analysis were conducted on the prepared samples to determine the surface area and pore characteristics (Figure 5). The surface area of the bare Cr_2O_3 was found to be about 23.83 m^2/g with a pore volume and pore diameter of 0.033 cm^3/g and 4.05 nm, respectively. Similarly, the BET surface area of pristine ZrO_2 nanoparticles was found to be about 14.74 m^2/g with a pore volume and diameter of 0.0012 cm^3/g and 2.90 nm, respectively. However, the Cr_2O_3/ZrO_2 nanocomposite exhibits an increased surface area of 38.43 m^2/g as well as a mid-way pore volume of 0.025 cm^3/g and pore diameter of 4.35 nm. The increased surface area and pore properties of the Cr_2O_3/ZrO_2 nanocomposite confirm that ZrO_2 nanoparticles have been dispersed onto the surface of Cr_2O_3 nanoparticles rather than intercalated into the lattice (Figure 5).

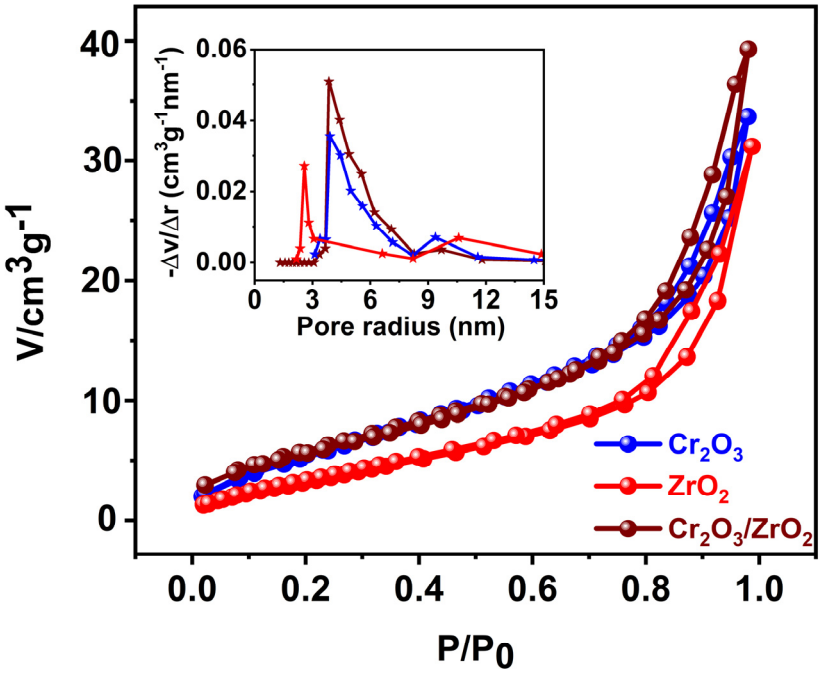

Figure 5. BET analysis spectra of Cr_2O_3, ZrO_2, and Cr_2O_3–ZrO_2 nanocomposites.

3.2. Catalytic Degradation of TCL and Pathway of the Cr_2O_3-ZrO_2 Composite

The photocatalytic degradation of TCL via the as-prepared Cr_2O_3-ZrO_2 composite has been carried out on a laboratory-designed photoreactor (Figure 6). Firstly, the effect of pH, in which three different values of pH 5 (acidic), pH 7 (neutral), and pH 9 (basic) were investigated to understand its influence on TCL degradation. The results indicated that all the pH levels showed higher efficiency in TCL degradation while the acidic pH showed the highest efficiency in TCL degradation after 120 min under visible light. The results indicated that the basic pH has significantly reduced the TCL degradation because at the basic pH the catalyst surface would be negatively charged, hence the unstable negatively charged TCL molecules would easily repel by the catalyst, thus the degradation has been decreased (Figure 6a). However, the acidic pH is more favorable for TCL degradation in which the surface attraction of the TCL molecule and the positively charged catalyst surface are higher to provide active sites and generate highly reactive organic species to degrade the TCL molecule under visible light [37,38]. To demonstrate the surface charge of the Cr_2O_3/ZrO_2 nanocomposite, the zeta potential analysis at various pH levels was measured to elucidate the isoelectric point of the photocatalyst, and, as shown in Figure S1, the composite has the isoelectric point at pH 6.22. The enhanced photocatalytic degradation of TCL at pH 5.0 is attributed to the strong electrostatic interaction of the positively charged surface of the Cr_2O_3/ZrO_2 photocatalyst, with the anionic tetracycline drug molecule. Beyond the isoelectric point (>6.22), the decline in photocatalytic drug degradation efficiency is attributed to the electrostatic repulsion between the negatively charged photocatalyst surface and the anionic tetracycline drug molecules.

In addition, the effect of catalyst load on the degradation of TCL has also been analyzed during photodegradation. From the results, it indicated that in the dark, there is no significant reduction in TCL concentration due to physical adsorption on the catalyst. Meanwhile, the degradation efficiency has been increased with the increase in the amount of the catalyst from 0.25 g/L to 1.0 g/L. However, subsequently, the efficiency has declined with the increase in catalyst load to 2.0 g/L (Figure 6b). This could be because with the increase in the catalyst load after the optimum ratio, the viscosity of the suspension would increase and subsequently decreases the light penetration onto the catalyst. This could lead to a reduction in light availability for the active sites of the catalyst, which could significantly decrease the degradation efficiency [39]. Thus, it was found that 1.0 g/L

of the catalyst was the optimum catalyst load for the enhanced TCL degradation under visible light.

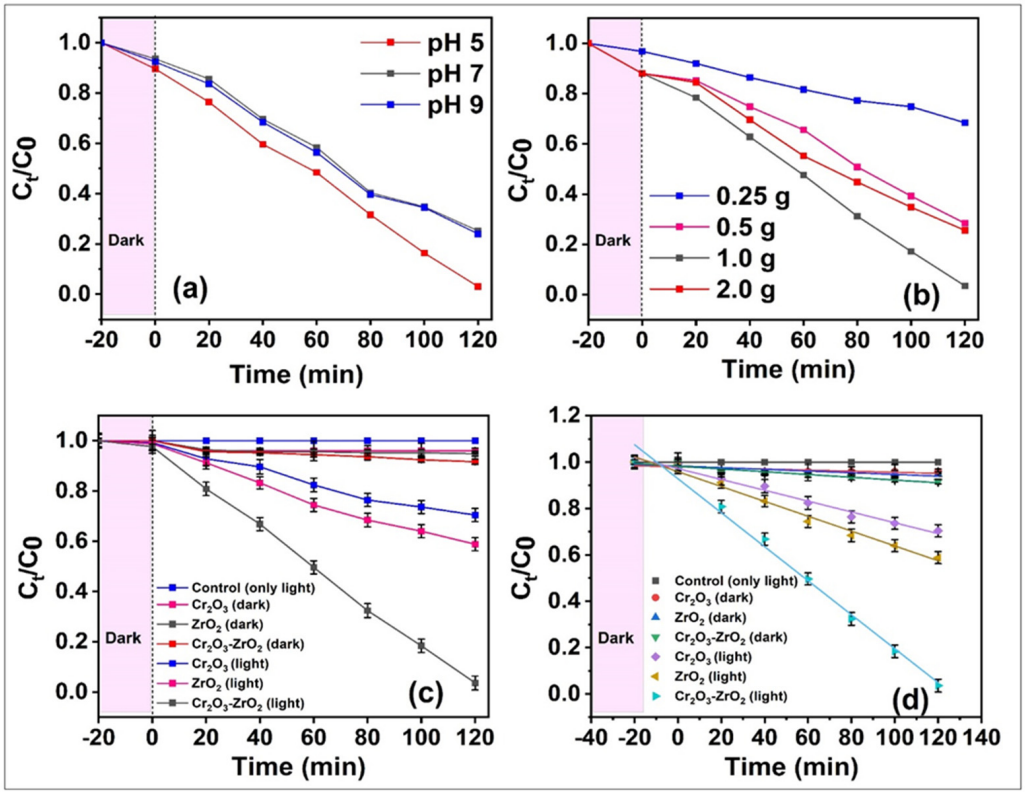

Figure 6. Influence of, (**a**) solution pH, (**b**) photocatalyst quantity, (**c**,**d**) degradation kinetics of TCL molecules under optimized experimental conditions.

From the above results, it is observed that at the optimum conditions the composite exhibited about 97.2% of TCL degradation in 120 min. It is worth mentioning that the pure Cr_2O_3 and ZrO_2 showed insignificant degradation efficiency in TCL degradation (Figure 6c,d). This could be because the energy band gap of Cr_2O_3 is too low which leads to the absorption of the visible light more easily to generate charge carriers, however, the recombination rate is significantly higher. Similarly, ZrO_2 has a slightly higher energy band gap, which is insufficient to generate photo-induced charge carriers. Thus, the composite has obtained an optimum energy band gap in which the photogenerated charge carriers would easily transfer to generate active radical species like $OH^{\bullet -}$ and $O_2^{\bullet -}$ to degrade the TCL to a lower molecule.

Furthermore, the plausible degradation pathway of TCL by the Cr_2O_3/ZrO_2 nanocomposite at the optimized conditions was investigated by LC-ESI/MS analysis (Figure 7). The results showed that there could reasonably be three sites to be attacked by the reactive oxygen species ($OH^{\bullet -}$ or $O_2^{\bullet -}$). Initially, the hydroxyl radical attacks the amine group and breaks the bond to form DP-1 (m/z = 430); similarly, in the other way, it could be attacked by the super oxide anion to form DP-2 (m/z = 490). Furthermore, the degradation products undergo effective attack by the hydroxyl radical to form hydroxylated compounds (DP-3, DP-4, and DP-5). Eventually, after formation of hydroxylated compounds, they further undergo an effective attack by both the hydroxyl and superoxide anion radicals to form ring opening structures (DP-8 to DP-12), which would further mineralize to generate smaller mineral acids, H_2O and CO_2.

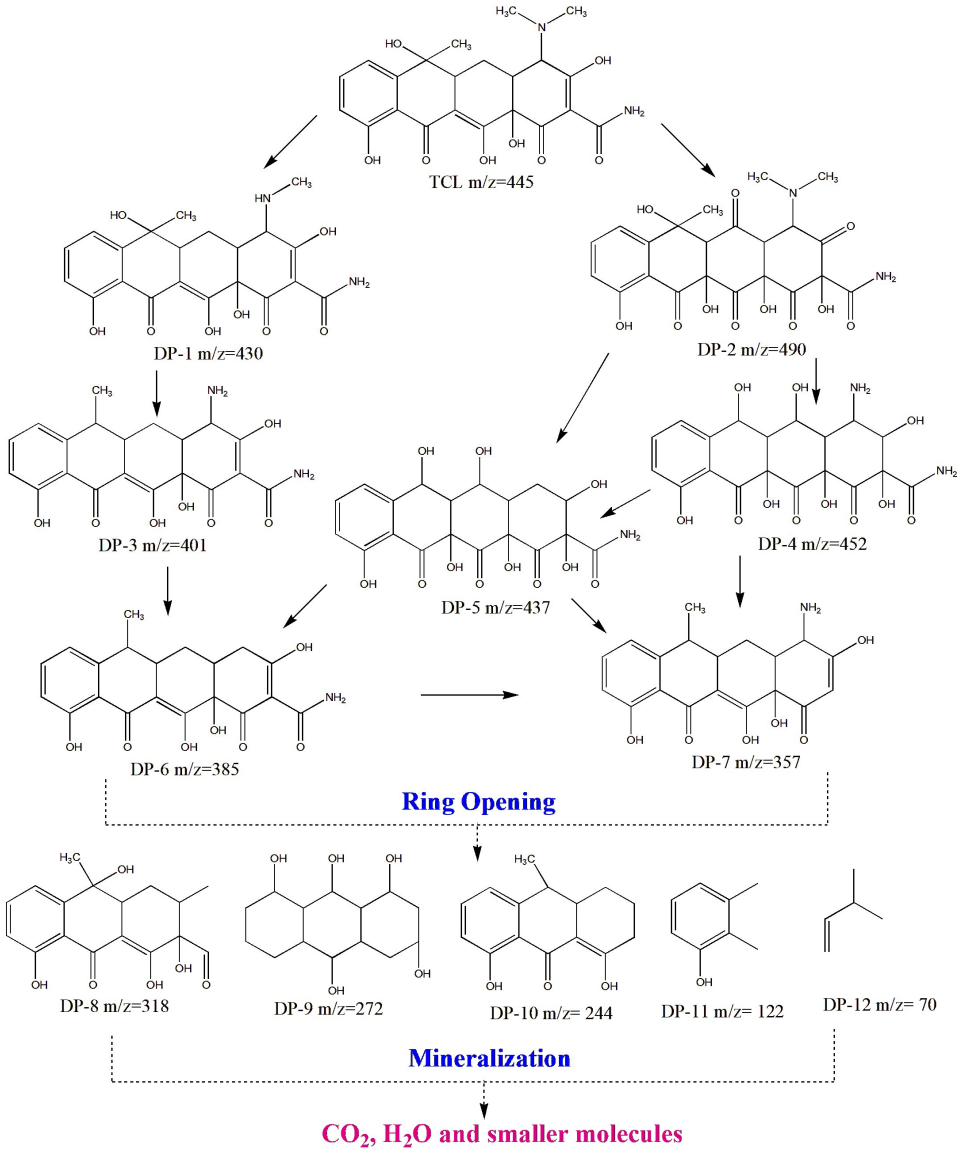

Figure 7. Plausible photocatalytic degradation pathway of TCL by Cr_2O_3/ZrO_2.

3.3. Photocatalysis Degradation Mechanism

To understand the possible reactive oxygen species involved in the degradation, a series of radical trapping and quantification experiments was carried out. The results indicated that after the addition of isopropyl alcohol ($OH^{\bullet-}$ scavenger) the degradation efficiency of TCL was significantly reduced, while benzoquinone ($O_2^{\bullet-}$ scavenger) has less influence than isopropyl alcohol on the TCL degradation. Furthermore, the addition of triethanolamine (h+ scavenger) had a slightly lower influence on the TCL degradation (Figure 8a). These phenomena were further supported by the radical quantification results (Figure 8b,c) (Figure S2) and confirmed that the $OH^{\bullet-}$ and $O_2^{\bullet-}$ species generation was increased with the increase in irradiation time and produced more species to be involved in TCL degradation.

Furthermore, the photocatalytic degradation mechanism of TCL by the Cr_2O_3/ZrO_2 composite was proposed and is shown in Figure 9. It is feasible to propose a traditional heterojunction-type photocatalytic mechanism for Cr_2O_3 and ZrO_2 since these semiconductors can form a unique p-n heterojunction structure. Upon visible light illumination, it is possible for electrons from the valence band (VB) of Cr_2O_3 to become excited to the conduction band (CB) of Cr_2O_3, creating holes. Meanwhile, the matched energy between ZrO_2 and Cr_2O_3 allows for the migration of photogenerated electrons from Cr_2O_3 CB to ZrO_2

CB, which produces superoxide radicals via further reaction with the dissolved oxygen. In the similar way, the holes in the VB of ZrO_2 can be relocated to the VB of Cr_2O_3, allowing for the formation of hydroxyl radicals by the photochemical reactions. As a result, the probability of electron/hole recombination is considerably reduced, since electrons concentrate primarily on the CB of ZrO_2 while holes stay in the VB of Cr_2O_3. As a result of the reduced electron/hole recombination and the formation of reactive oxygen species, tetracycline drug molecules are mineralized into CO_2, H_2O, and other non-toxic compounds.

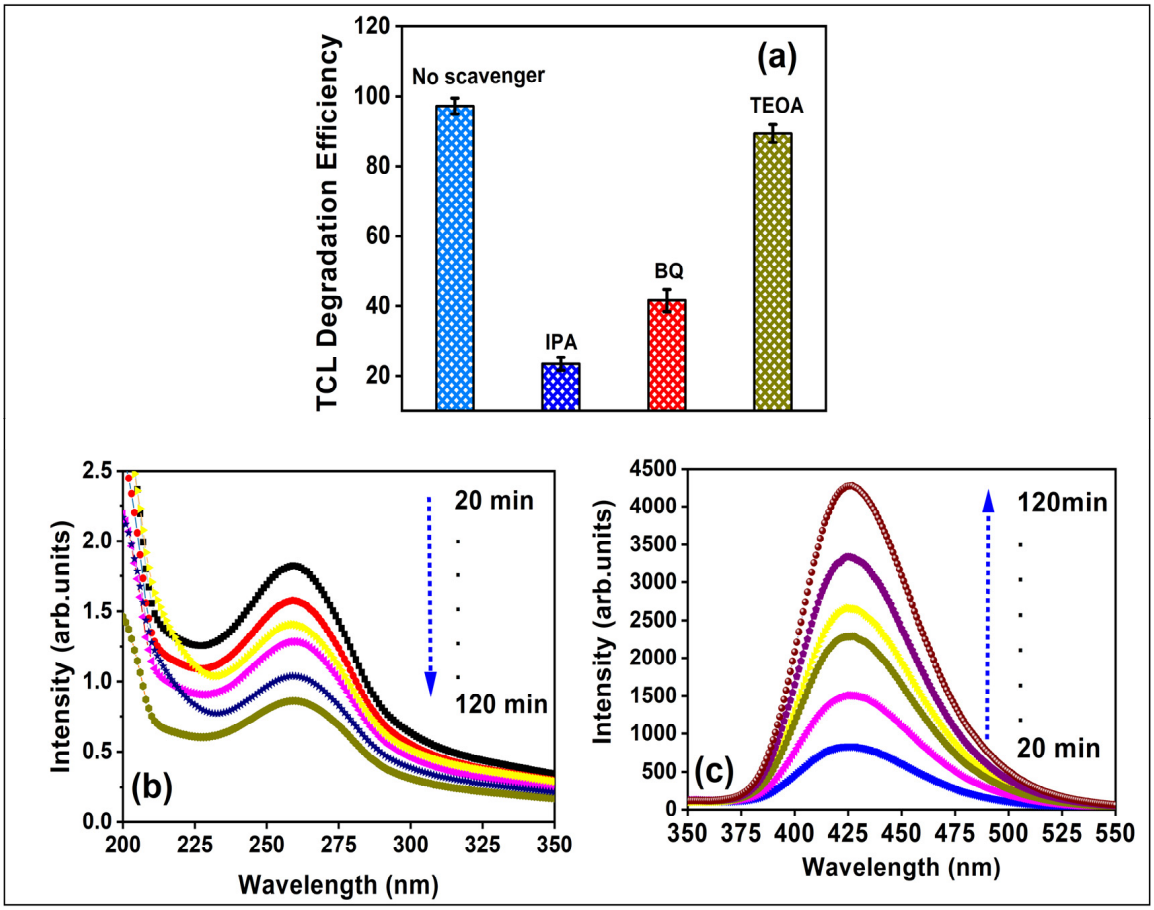

Figure 8. Radical quantification of (**a**) $O_2^{\bullet-}$ and (**b**) $OH^{\bullet-}$; (**c**) photocatalytic efficiency of nanocomposite in the presence of different trapping agents.

In addition, the recycle test has also been performed by centrifuging the used catalyst at 5000 rpm for 5 min and collected, followed by drying at 60 °C before using it in the next cycle. From the results, as shown in Figure 10a, the proposed nanocomposite materials can undergo six successive cycles without losing their photocatalytic efficiency. In addition, the XRD results reveals an unaltered crystallinity along with retention of the structural characteristics of the photocatalyst even after six cycles of usage (Figure 10b). The superior performance of the proposed photocatalyst has been compared with similar type of photocatalysts reported in the literature [32–39], and the observations are described in Table 1.

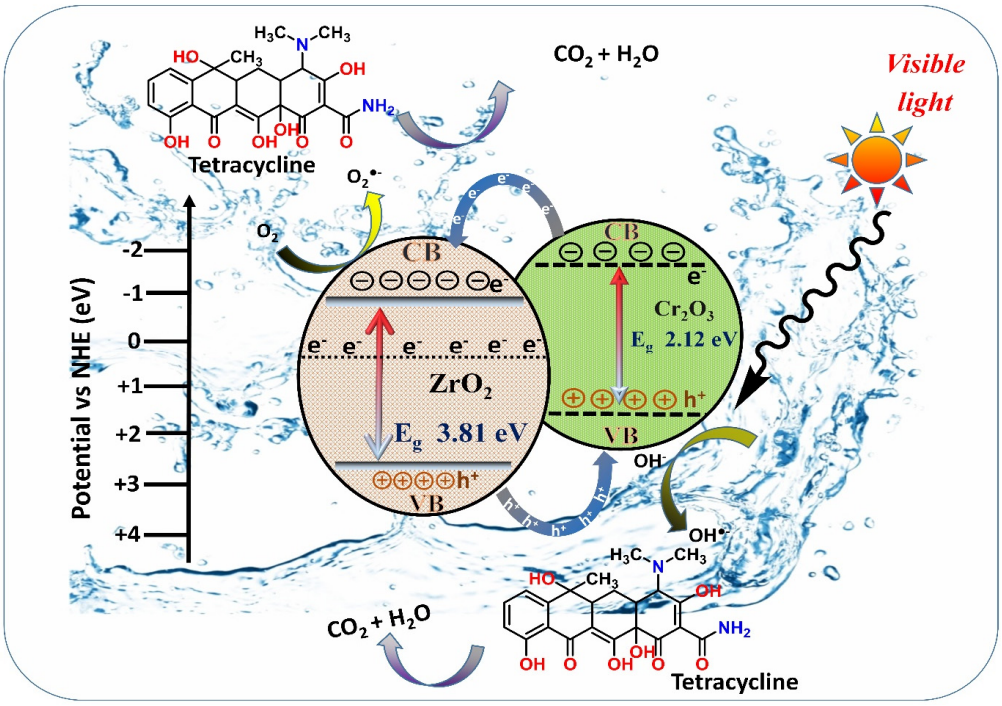

Figure 9. Photocatalytic mechanism of Cr_2O_3–ZrO_2 nanocomposite under visible light.

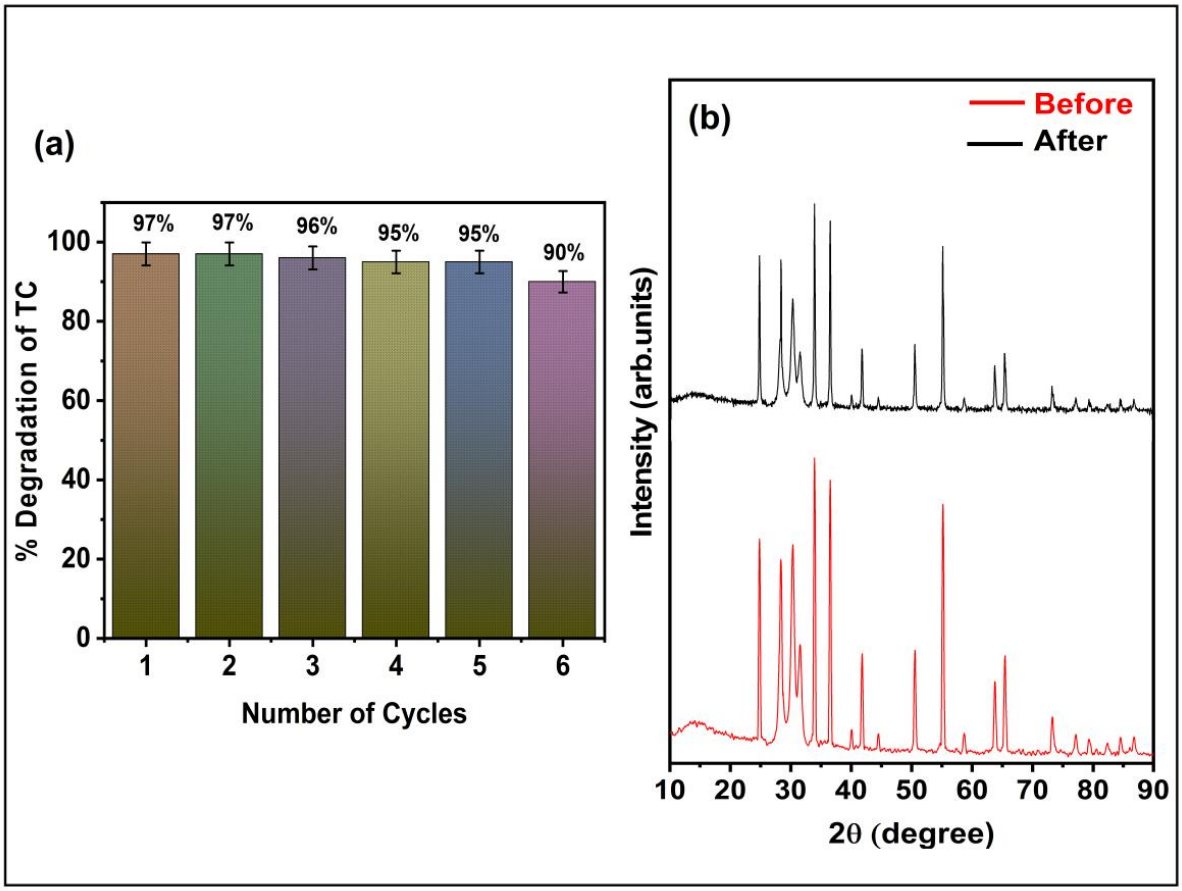

Figure 10. (**a**) Reusability studies and (**b**) XRD analysis of Cr_2O_3–ZrO_2 nanocomposite under optimized experimental conditions.

Table 1. Comparison of literature reports on the degradation of tetracycline drug with the proposed method.

S. No.	Photocatalyst	Light Source	Degradation Time	Degradation (%)	Catalyst Amount (mg)	Drug Conc. (mg/L)	Ref.
1.	α-Fe_2O_3/g-C_3N_4 NCs	Visible (32 mW/cm^2, W)	180 min	95.0	50	10	[40]
2.	Black Phosphorus/BiOBr NCs	Visible (300 W/cm^2, Xe)	90 min	79.0	100	50	[41]
3.	$BiWO_6$	Visible (300 W/cm^2, Xe)	180 min	79.7	30	20	[42]
4.	WO_3/g-C_3N_4	Visible (300 W/cm^2, Xe)	60 min	78.0	50	80	[43]
5.	(Bi)BiOBr/rGO NCs	Visible (300 W/cm^2, Xe)	140 min	98.0	50	20	[44]
6.	Ni-WO_3	LED (35W)	105 min	76.0	50	10	[45]
7.	$BiVO_4$/Fe_2O_3	Visible (300 W/cm^2, Xe)	60 min	91.5	30	15	[46]
8.	CuS/CdS NCs	Solar Light	50 min	90.0	50	20	[47]
9.	Cr_2O_3/ZrO_2	Visible (300 W/cm^2, Xe)	120 min	97.1	100	50	Present Work

4. Conclusions

A novel Cr_2O_3–ZrO_2 nanocomposite has been successfully synthesized for the efficient degradation of the tetracycline antibiotic under visible light. Our results indicated that the ZrO_2 nanoparticles were uniformly distributed on the Cr_2O_3 cubes which facilitates a strong interaction to form a heterojunction which further leads to improving the charge separation rate and reducing the recombination rate. Furthermore, the composite showed enhanced degradation efficiency towards TCL, which was about 97.1% after 120 min of visible light irradiation at the optimal conditions (pH = 5, catalyst load = 0.1 gL^{-1}, and TCL concentration = 50 mgL^{-1}). The radical trapping and the active species scavenging experimental results revealed that the $OH^{\bullet -}$, $O_2^{\bullet -}$, and photogenerated holes are the main species involved in the TCL degradation. Thus, our study suggests new insights into the preparation of Cr- and Zr-based metal oxide heterojunctions with efficient visible light harvesting capabilities for degradation of antibiotic pollutants under visible light during pharmaceutical wastewater treatment processes.

Supplementary Materials: The following supporting information can be downloaded at: https://www.mdpi.com/article/10.3390/w15203702/s1, Figure S1: Zeta potential vs. pH for Cr_2O_3-ZrO_2 nanocomposite; Figure S2: (a) Reaction pathway between terepthalic acid and hydroxyl radical with the formation of fluorescent 2-hydroxy terepthalic acid (b) Reaction pathway between NBT and superoxide radicals with the formation of formazan.

Author Contributions: Conceptualization, X.W. and S.N.; methodology, X.W. and S.N.; validation, X.W. and P.C.; resources, J.L. and B.L.; writing—original draft preparation, X.W.; writing—review and editing, X.W., X.Y. and S.N.; visualization, X.W.; funding acquisition, X.W. and S.N. All authors have read and agreed to the published version of the manuscript.

Funding: This research was funded by the Anhui Polytechnic University Introduction of Talents Research Start-up Fund (Grant No: 2023YQQ011), Natural Science Key Foundation of Educational Commission of Anhui Province (Grant No. 2022AH050989) and Scientific Research Project of Anhui Polytechnic University (Grant No. Xjky2022170).

Data Availability Statement: Data are available from the corresponding author on request.

Conflicts of Interest: The authors declare no conflict of interest.

References

1. Dong, Y.; Xu, D.; Zhang, J.; Wang, Q.; Pang, S.; Zhang, G.; Campos, L.C.; Lv, L.; Liu, X.; Gao, W.; et al. Enhanced antibiotic wastewater degradation by intimately coupled B-Bi_3O_4Cl photocatalysis and biodegradation reactor: Elucidating degradation principle systematically. *J. Hazard. Mater.* **2023**, *445*, 130364. [CrossRef] [PubMed]
2. Yu, Y.; Hu, X.; Li, M.; Fang, J.; Leng, C.; Zhu, X.; Xu, W.; Qin, J.; Yao, L.; Liu, Z.; et al. Constructing mesoporous Zr-doped SiO_2 onto efficient Z-scheme TiO_2/g-C_3N_4 heterojunction for antibiotic degradation via adsorption-photocatalysis and mechanism insight. *Environ. Res.* **2022**, *214*, 114189. [CrossRef] [PubMed]
3. Li, J.; Li, Y.; Zhu, M.; Mei, Q.; Tang, X.; Wu, Y.; Yue, S.; Tang, Y.; Wang, Q. Constructing aloe-emodin/FeOOH organic-inorganic heterojunction for synergetic photocatalysis-Fenton eliminating antibiotic pollutants. *J. Environ. Chem. Eng.* **2023**, *11*, 109775. [CrossRef]
4. Sharma, M.; Mandal, M.K.; Pandey, S.; Kumar, R.; Dubey, K.K. Visible-Light-Driven Photocatalytic Degradation of Tetracycline Using Heterostructured Cu_2O-TiO_2 Nanotubes, Kinetics, and Toxicity Evaluation of Degraded Products on Cell Lines. *ACS Omega* **2022**, *7*, 33572–33586. [CrossRef] [PubMed]
5. Wu, S.; Hu, H.; Lin, Y.; Zhang, J.; Hu, Y.H. Visible light photocatalytic degradation of tetracycline over TiO_2. *Chem. Eng. J.* **2020**, *382*, 122842. [CrossRef]
6. Li, C.; Tian, Q.; Zhang, Y.; Li, Y.; Yang, X.; Zheng, H.; Chen, L.; Li, F. Sequential combination of photocatalysis and microalgae technology for promoting the degradation and detoxification of typical antibiotics. *Water Res.* **2022**, *210*, 117985. [CrossRef] [PubMed]
7. Ji, B.; Zhang, J.; Zhang, C.; Li, N.; Zhao, T.; Chen, F.; Hu, L.; Zhang, S.; Wang, Z. Vertically Aligned ZnO@ZnS Nanorod Chip with Improved Photocatalytic Activity for Antibiotics Degradation. *ACS Appl. Nano Mater.* **2018**, *1*, 793–799. [CrossRef]
8. Naraginti, S.; Yu, Y.Y.; Fang, Z.; Yong, Y.C. Novel tetrahedral Ag_3PO_4@N-rGO for photocatalytic detoxification of sulfamethoxazole: Process optimization, transformation pathways and biotoxicity assessment. *Chem. Eng. J.* **2019**, *375*, 122035. [CrossRef]
9. Tan, R.; Wang, Y.; Jin, Z.; Zhang, P.; Luo, H.; Liu, D.; Mamba, B.B.; Kuvarega, A.T.; Gui, J. Preparation of carbon-coated brookite@anatase TiO_2 heterophase junction nanocables with enhanced photocatalytic performance. *Photochem. Photobiol. Sci.* **2020**, *19*, 966–975. [CrossRef]
10. Sompalli, N.K.; Mohanty, A.; Mohan, A.M.; Deivasigamani, P. Heterojunction Cr_2O_3-Ag_2O nanocomposite decorated porous polymer monoliths a new class of visible light fast responsive heterogeneous photocatalysts for pollutant clean-up. *J. Environ. Chem. Eng.* **2021**, *9*, 104846. [CrossRef]
11. Sompalli, N.K.; Das, A.; De, S.S.; Mohan, A.M.; Deivasigamani, P. Mesoporous monolith designs of mixed phased titania codoped Sm^{3+}/Er^{3+} composites: A super responsive visible light photocatalysts for organic pollutant clean-up. *Appl. Surf. Sci.* **2020**, *504*, 144350. [CrossRef]
12. Yang, X.; Wang, D. Photocatalysis: From Fundamental Principles to Materials and Applications. *ACS Appl. Energy Mater.* **2018**, *1*, 6657–6693. [CrossRef]
13. Wen, Y.; Feng, M.; Zhang, P.; Zhou, H.-C.; Sharma, V.K.; Ma, X. Metal Organic Frameworks (MOFs) as Photocatalysts for the Degradation of Agricultural Pollutants in Water. *ACS ES&T Eng.* **2021**, *1*, 804–826. [CrossRef]
14. Li, Y.; Chen, F.; Wang, Y.; Tang, N.; He, R. *Semiconductor Photocatalysis for Water Purification*; Elsevier Inc.: Amsterdam, The Netherlands, 2019. [CrossRef]
15. Elaheh, K.; Naimeh, S. *The Application of Photocatalytic Materials for Efficient Air Purification*; Elsevier Inc.: Amsterdam, The Netherlands, 2020. [CrossRef]
16. Oluwole, A.O.; Olatunji, O.S. Photocatalytic degradation of tetracycline in aqueous systems under visible light irridiation using needle-like SnO_2 nanoparticles anchored on exfoliated g-C_3N_4. *Environ. Sci. Eur.* **2022**, *34*, 5. [CrossRef]
17. Zhou, X.; Chen, X.; Han, W.; Han, Y.; Guo, M.; Peng, Z.; Fan, Z.; Shi, Y.; Wan, S. Tetracycline Removal by Hercynite-Biochar from the Co-Pyrolysis of Red Mud-Steel Slag-Sludge. *Nanomaterials* **2022**, *12*, 2595. [CrossRef] [PubMed]
18. Zhou, Q.; Hong, P.; Shi, X.; Li, Y.; Yao, K.; Zhang, W.; Wang, C.; He, J.; Zhang, K.; Kong, L. Efficient degradation of tetracycline by a novel nanoconfinement structure Cu_2O/Cu@MXene composite. *J. Hazard. Mater.* **2023**, *448*, 130995. [CrossRef] [PubMed]
19. Jia, K.; Liu, G.; Lang, D.N.; Chen, S.F.; Yang, C.; Wu, R.L.; Wang, W.; Wang, J.D. Fast photodegradation of antibiotics and dyes by an anionic surfactant-aided CdS/ZnO nanodispersion. *New J. Chem.* **2022**, *46*, 11303–11314. [CrossRef]
20. He, Y.; Wang, D.; Li, X.; Fu, Q.; Yin, L.; Yang, Q.; Chen, H. Photocatalytic degradation of tetracycline by metal-organic frameworks modified with Bi_2WO_6 nanosheet under direct sunlight. *Chemosphere* **2021**, *284*, 131386. [CrossRef]
21. He, X.; Kai, T.; Ding, P. Heterojunction Photocatalysts for Degradation of the Tetracycline Antibiotic: A Review. *Environ. Chem. Lett.* **2021**, *19*, 4563–4601. [CrossRef]
22. Singh, K.K.; Senapati, K.K.; Borgohain, C.; Sarma, K.C. Newly developed Fe_3O_4–Cr_2O_3 magnetic nanocomposite for photocatalytic decomposition of 4-chlorophenol in water. *J. Environ. Sci.* **2017**, *52*, 333–340. [CrossRef]
23. Ahmed, M.A.; Abou-Gamra, Z.M.; Salem, A.M. Photocatalytic degradation of methylene blue dye over novel spherical mesoporous Cr_2O_3/TiO_2 nanoparticles prepared by sol-gel using octadecylamine template. *J. Environ. Chem. Eng.* **2017**, *5*, 4251–4261. [CrossRef]
24. Mohanapandian, K.; Krishnan, A. Synthesis, structural, morphological and optical properties of Cu^{2+} doped Cr_2O_3 nanoparticles. *Int. J. Adv. Eng. Technol. E* **2016**, *7*, 273–279. Available online: http://www.technicaljournalsonline.com/ijeat/VOL%20VII/IJAET%20VOL%20VII%20ISSUE%20II%20APRIL%20JUNE%202016/20167250.pdf (accessed on 16 October 2023).

25. Rani, V.; Sharma, A.; Kumar, A.; Singh, P.; Thakur, S.; Singh, A.; Van Le, Q.; Nguyen, V.H.; Raizada, P. ZrO_2-Based Photocatalysts for Wastewater Treatment: From Novel Modification Strategies to Mechanistic Insights. *Catalysts* **2022**, *12*, 1418. [CrossRef]
26. Agorku, E.S.; Kuvarega, A.T.; Mamba, B.B.; Pandey, A.C.; Mishra, A.K. Enhanced visible-light photocatalytic activity of multi-elements-doped ZrO_2 for degradation of indigo carmine. *J. Rare Earths* **2015**, *33*, 498–506. [CrossRef]
27. Kadam, A.; Dhabbe, R.; Gophane, A.; Sathe, T.; Garadkar, K. Template free synthesis of ZnO/Ag_2O nanocomposites as a highly efficient visible active photocatalyst for detoxification of methyl orange. *J. Photochem. Photobiol. B Biol.* **2016**, *154*, 24–33. [CrossRef] [PubMed]
28. Aldeen, E.M.S.; Jalil, A.A.; Mim, R.S.; Alhebshi, A.; Hassan, N.S.; Saravanan, R. Altered zirconium dioxide based photocatalyst for enhancement of organic pollutants degradation: A review. *Chemosphere* **2022**, *304*, 135349. [CrossRef] [PubMed]
29. Yazdi, M.N.; Yamini, Y.; Asiabi, H. Multiwall carbon nanotube-zirconium oxide nanocomposite hollow fiber solid phase microextraction for determination of polyaromatic hydrocarbons in water, coffee and tea samples. *J. Chromatogr. A* **2018**, *1554*, 8–15. [CrossRef]
30. Ivanova, T.; Gesheva, K.; Cziraki, A.; Szekeres, A.; Vlaikova, E. Structural transformations and their relation to the optoelectronic properties of chromium oxide thin films. *J. Phys. Conf. Ser.* **2008**, *113*, 012030. [CrossRef]
31. Ocaa, M. Nanosized Cr_2O_3 hydrate spherical particles prepared by the urea method. *J. Eur. Ceram. Soc.* **2001**, *21*, 931–939. [CrossRef]
32. Jagadeesan, D.; Sompalli, N.K.; Mohan, A.M.; Rao, C.V.S.B.; Nagarajan, S.; Deivasigamani, P. ZrO_2–Ag_2O nanocomposites encrusted porous polymer monoliths as high-performance visible light photocatalysts for the fast degradation of pharmaceutical pollutants. *Photochem. Photobiol. Sci.* **2022**, *21*, 1273–1286. [CrossRef]
33. Kadari, A.; Schemme, T.; Kadri, D.; Wollschläger, J. XPS and morphological properties of Cr_2O_3 thin films grown by thermal evaporation method. *Results Phys.* **2017**, *7*, 3124–3129. [CrossRef]
34. Cao, Z.; Zuo, C. Cr_2O_3/carbon nanosheet composite with enhanced performance for lithium ion batteries. *RSC Adv.* **2017**, *7*, 40243–40248. [CrossRef]
35. Liu, J.; Liao, M.; Imura, M.; Tanaka, A.; Iwai, H.; Koide, Y. Low on-resistance diamond field effect transistor with high-k ZrO_2 as dielectric. *Sci. Rep.* **2014**, *4*, 2–6. [CrossRef]
36. Luo, J.; Luo, X.; Hu, C.; Crittenden, J.C.; Qu, J. Zirconia (ZrO_2) Embedded in Carbon Nanowires via Electrospinning for Efficient Arsenic Removal from Water Combined with DFT Studies. *ACS Appl. Mater. Interfaces* **2016**, *8*, 18912–18921. [CrossRef] [PubMed]
37. Divakaran, K.; Baishnisha, A.; Balakumar, V.; Perumal, K.N.; Meenakshi, C.; Kannan, R.S. Photocatalytic degradation of tetracycline under visible light using TiO_2@ sulfur doped carbon nitride nanocomposite synthesized via in-situ method. *J. Environ. Chem. Eng.* **2021**, *9*, 105560. [CrossRef]
38. McGrady, J.; Yamashita, S.; Kano, S.; Yang, H.; Abe, H. Charge transfer across the Cr_2O_3, Fe_2O_3, and ZrO_2 oxide/water interface: A pulse radiolysis study. *Radiat. Phys. Chem.* **2021**, *180*, 109240. [CrossRef]
39. Safari, G.; Hoseini, M.; Seyedsalehi, M.; Kamani, H.; Jaafari, J.; Mahvi, A. Photocatalytic degradation of tetracycline using nanosized titanium dioxide in aqueous solution. *Int. J. Environ. Sci. Technol.* **2015**, *12*, 603–616. [CrossRef]
40. Linh, N.X.D.; Hanh, N.T.; Cuong, L.M.; Huong, N.T.; Ha, N.T.T.; Trinh, T.D.; Van Noi, N.; Cam, N.T.D.; Pham, T.D. Facile Fabrication of α-Fe_2O_3/g-C_3N_4 Z-Scheme Heterojunction for Novel Degradation of Residual Tetracycline. *Top. Catal.* **2023**, *66*, 139–148. [CrossRef]
41. Li, X.; Xiong, J.; Gao, X.; Ma, J.; Chen, Z.; Kang, B.; Liu, J.; Li, H.; Feng, Z.; Huang, J. Novel BP/BiOBr S-scheme nano-heterojunction for enhanced visible-light photocatalytic tetracycline removal and oxygen evolution activity. *J. Hazard. Mater.* **2020**, *387*, 121690. [CrossRef]
42. Chen, L.; Xu, B.; Jin, M.; Chen, L.; Yi, G.; Xing, B.; Zhang, Y.; Wu, Y.; Li, Z. Excellent photocatalysis of Bi_2WO_6 structured with oxygen vacancies in degradation of tetracycline. *J. Mol. Struct.* **2023**, *1278*, 134911. [CrossRef]
43. Pan, T.; Chen, D.; Xu, W.; Fang, J.; Wu, S.; Liu, Z.; Wu, K.; Fang, Z. Anionic polyacrylamide-assisted construction of thin 2D-2D WO_3/g-C_3N_4 Step-scheme heterojunction for enhanced tetracycline degradation under visible light irradiation. *J. Hazard. Mater.* **2020**, *393*, 122366. [CrossRef]
44. Jiang, H.; Wang, Q.; Chen, P.; Zheng, H.; Shi, J.; Shu, H.; Liu, Y. Photocatalytic degradation of tetracycline by using a regenerable (Bi)BiOBr/rGO composite. *J. Clean. Prod.* **2022**, *339*, 130771. [CrossRef]
45. Phuong, D.M.; Duong, T.A.; Huong, N.T.; Khoa, N.V.; Hanh, N.T.; Phuong, N.M.; Pham, T.D.; Trang, H.T.; Van Noi, N. Enhancement of visible light photocatalytic removal of residual tetracycline by Ni doped WO_3 nano structures. *Inorg. Chem. Commun.* **2023**, *157*, 111329. [CrossRef]
46. Fu, Q.; Meng, Y.; Yao, Y.; Shen, H.; Xie, B.; Ni, Z.; Xia, S. Construction of facet orientation-supported Z-scheme heterojunction of $BiVO_4$ (110)-Fe_2O_3 and its photocatalytic degradation of tetracycline. *J. Environ. Chem. Eng.* **2023**, *11*, 111060. [CrossRef]
47. Siddhardhan, E.V.; Surender, S.; Arumanayagam, T. Degradation of tetracycline drug in aquatic environment by visible light active CuS/CdS photocatalyst. *Inorg. Chem. Commun.* **2023**, *147*, 110244. [CrossRef]